electronics

Article

An Analysis and Modeling of the Class-E Inverter for ZVS/ZVDS at Any Duty Ratio with High Input Ripple Current

Ratil H. Ashique [1,*], ASM Shihavuddin [1], Mohammad Monirujjaman Khan [2], Aminul Islam [3], Jubaer Ahmed [4], M. Saad Bin Arif [5], Md Hasan Maruf [1], Ahmed Al Mansur [1], Mohammad Asif ul Haq [1] and Ashraf Siddiquee [1]

[1] Department of Electrical and Electronic Engineering, Green University of Bangladesh, Dhaka 1207, Bangladesh; shihav@eee.green.edu.bd (A.S.); maruf@eee.green.edu.bd (M.H.M.); mansur@eee.green.edu.bd (A.A.M.); asiful@eee.green.edu.bd (M.A.u.H.); ashraf@eee.green.edu.bd (A.S.)

[2] Department of Electrical and Computer Engineering, North South University, Dhaka 1229, Bangladesh; monirujjaman.khan@northsouth.edu

[3] Department of Mechanical Engineering, Technical University of Denmark, 2800 Kgs. Lyngby, Denmark; mais@mek.dtu.dk

[4] Department of Electrical and Electronic Engineering, Swinburne University of Technology Malaysia, Sarawak 93350, Malaysia; JAhmed@swinburne.edu.my

[5] Department of Electrical and Electronic Engineering, Aligarh Muslim University, Uttar Pradesh 202002, India; saad.ee@amu.ac.in

* Correspondence: ratil@eee.green.edu.bd

Abstract: This paper presents an analysis and modeling of the class-E inverter for ZVS/ZVDS execution at any duty ratio. The methodology is to determine the input current to the inverter analytically under the assumption that it always remains positive. The latter is ensured by proper selection of the input inductance such that the inverter always operates either in (1) the border condition mode or in (2) the continuous conduction mode regardless of the input ripple. Using this input current and applying the boundary conditions, the required input capacitance for the ZVS/ZVDS execution is determined at a specified input/output voltage, output power and load. The analysis shows that the ZVS/ZVDS can be achieved while the input capacitance is selected appropriately. A comparison between the analytical and simulation results is also formulated involving the proposed and other existing models. The simulation results that are provided at different duty ratios demonstrate that they are in a better agreement with the proposed analytical model regardless of the input inductance and the state of input ripple current. The analytical modeling is facilitated by using MAPLE®.

Keywords: Class E; Class EF2; Class E/F3; ZVS; Soft Switching

1. Introduction

The class-E inverter has found numerous applications in radio transmission, induction heating, industrial ultrasonic, renewable energy systems or commercial electronics industry [1–5]. In that regard, many application-specific designs are also proposed [3–7]. The widespread adoption of this inverter is mainly due to the compact topology with low component count and the capability of the circuit to deliver high power. On top of that, it can operate at high switching frequency with high efficiency if coupled with the zero-voltage switching (ZVS) or zero derivative voltage switching (ZVDS) techniques. The analysis and modeling of the ZVS/ZVDS class-E inverters are well reported in the literature [1–16]. Some of these modeling techniques are described here [1,2,8,11,12]. These techniques assume that the resonant current is sinusoidal, and, most importantly, the input current is a pure dc with very low ac component. The latter can be achieved if the input inductance is kept sufficiently large. Consequently, these models can define the behavior of the input current with the change in duty ratio. However, at lower inductances

and higher ripple current, the assumption is no longer valid. The input current to the inverter is dependent on the input inductance, the input capacitance along with the duty ratio of the circuit. Consequently, the existing modeling techniques [1–9,12–16]. fail to define the input current accurately. This inaccuracy further leads to miscalculation of the input/output power and the efficiency of the circuit. Henceforth, this work proposes an input current–based modeling of the class-E inverter. This proposed modeling technique has the following key features:

(1) It provides an analysis and modeling of the class-E ZVS/ZVDS inverter for any duty ratio.

(2) More accurate modeling of the input current, regardless of the input inductance and input ripple current. This feature helps to determine the input power and efficiency more accurately.

(3) The model can ensure the ZVS/ZVDS operation at any given load.

In the following sections, this model is discussed, analyzed and compared with the simulated results. The analytical modeling presented is performed using MAPLE®.

2. The Circuit Operation of Class-E Inverter

The topology of the class-E inverter is given in Figure 1. The inductance Lr and the capacitance C_r is chosen to resonate at f_r, which is also the switching frequency of the inverter. The L_f can be chosen to provide a constant dc current. However, the input ripple current percentage will increase with the decreasing size of the inductance L_f. The input capacitance C_{in} is inclusive of any parasitic drain to source capacitance of the switch and any external capacitance added. The switch S1 is operated with a duty ratio D. The switching pattern is given as follows.

$$Switch = \begin{cases} Turned\ ON, & 0 \leq \theta < 2\pi D \\ Turned\ OFF, & 2\pi D \leq< \theta < 2\pi \end{cases}$$
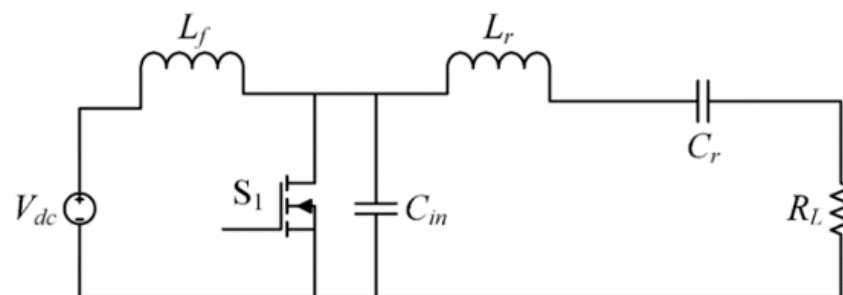

Figure 1. The class-E inverter.

2.1. Modes of Operation

The circuit is operated in two modes. In mode 1, the switch is turned ON and the voltage across the capacitor C_{in} falls to zero. The input current flows through the switch S1 and the L_f is charged. In the resonant tank, resonant current flows to the switch direction exchanging stored energy from C_r to L_r and completing half of the resonance cycle. This is shown in Figure 2a. In mode 2 (Figure 2b), the switch S1 is turned off and the input current I_{in} is diverted to the input capacitance C_{in}. At this moment, the input capacitor is charged to the peak switch voltage. Subsequently, it is discharged to zero at the end of this mode aiding in ZVS/ZVDS turn on of S1. If we assume the switch voltage is vs (θ), the following conditions must be satisfied in order to achieve ZVS or ZVDS:
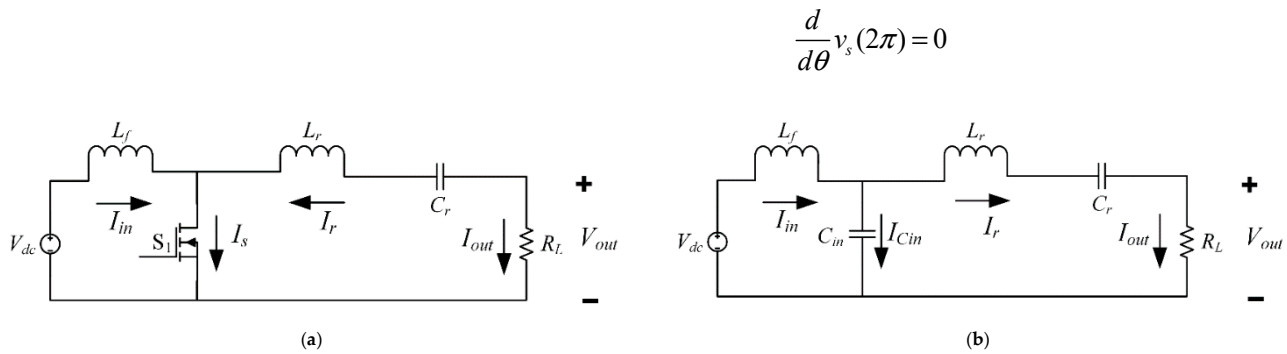
$$v_s(2\pi) = 0$$

and

$$\frac{d}{d\theta}v_s(2\pi) = 0$$

(**a**)   (**b**)

Figure 2. The class-E converter in (**a**) Mode 1 (**b**) Mode 2.

The class-E inverter operating modes are shown in Figure 2. The current through the switch diverts to charge the input capacitor C_{in} when the switch is closed at $\theta = 2\pi D$. As soon as C_{in} is charged completely, the current alters direction and C_{in} discharges. Due to the inductive effect of the resonant tank in Mode 2, the output current (I_{out}) lags the output voltage (V_{out}).

2.2. Assumptions

The circuit analysis is performed by applying the following assumptions.

a.   All the components are ideal and do not possess any parasitic resistance or capacitances.

b.   The switch is ideal. It is an open circuit ($v_s = \infty$) while OFF and shorted ($v_s = 0$) while ON.

c.   The input current (I_{in}) is always positive.

3. The Circuit Modeling

3.1. Modeling Approach

Given,

$$N = \frac{L_f}{L_{f\_boundary}}$$

where, $L_{f\_boundary}$ = boundary value of the input inductor (L_f) while the inverter operates at the border condition mode (BCM) and N = inductance ratio.

Now, the modeling approach is stated as follows

Step 1: To determine the switch voltage ($v_s(\theta)$)

Step 2: To apply the boundary conditions for ZVS/ZVDS and find input current ($I_{in}(\theta)$)

Step 3: To find $L_{f\_boundary}$ and the input ripple current (Δi_{in})

Step 4:

   Case 1 (N ≈ 1)

      (1) To determine the average input current ($I_{in\_avg\_case1}$)

      (2) Using $I_{in\_avg\_case1}$ to find the input capacitance (C_{in_case1})

   Case 2 (1.5 < N < 3)

      (1) To determine the average input current ($I_{in\_avg\_case2}$)

      (2) Using $I_{in\_avg\_case2}$ to find the input capacitance (C_{in_case2})

   Case 3 (N ≥ 3)

      (1) To determine the average input current ($I_{in\_avg\_case3}$)

      (2) Using $I_{in\_avg\_case3}$ to find the input capacitance (C_{in_case3})

Step 5: To find the peak switch voltage (v_{s_pk}) and the peak switch current (i_{s_pk})

3.2. *The Derivation*

3.2.1. Step 1

If the current through the input capacitor (C_{in}) is I_{Cin}, the switch voltage can be expressed as

$$v_s(\theta) = \frac{1}{\omega C_{in}} \int_{2\pi D}^{\theta} I_{Cin} d\theta \qquad (1)$$

From Figure 2a, the input current I_{in} can be written as

$$I_{in}(\theta) = I_{Cin}(\theta) + I_r(\theta) \qquad (2)$$

where

$I_r(\theta)$ is the resonant current;
I_{Cin} is the capacitor current;
$I_{in}(\theta)$ is the input current.

From (1),

$$v_s(\theta) = \frac{1}{\omega C_{in}} \int_{2\pi D}^{\theta} (I_{in\_avg} - I_m \sin(\theta + \varphi)) d\theta \qquad (3)$$

Simplifying,

$$v_s(\theta) = \frac{-2I_{in\_avg}\pi D - I_m \cos(2\pi D + \varphi) + I_{in\_avg}\theta + I_m \cos(\theta + \varphi)}{\omega C_{in}} \qquad (4)$$

3.2.2. Step 2

Applying $v_s(2\pi) = 0$ for ZVS to (4),

$$I_m = \frac{2\pi I_{in\_avg}(1 - D)}{\cos(2\pi D + \varphi) - \cos\varphi} \qquad (5)$$

or,

$$I_{in\_avg} = \frac{I_m(\cos(2\pi D + \varphi) - \cos\varphi)}{2\pi(1 - D)} \qquad (6)$$

Again, applying $v_s(2\pi) = 0$ and using (5) and (6),

$$\varphi = \pi + \arctan\left(\frac{\cos(2\pi D) - 1}{2\pi(1 - D) + \sin(2\pi D)}\right) \qquad (7)$$

Now, replacing (6) into (4) and simplifying (A1) (see Appendix A) is obtained. The output power to the load is defined by

$$P_{out,rms} = \left(\frac{I_m}{\sqrt{2}}\right)^2 R_L \qquad (8)$$

or

$$I_m = \sqrt{\frac{2P_{out,rms}}{R_L}} \qquad (9)$$

where R_L is the given load resistance. Now, replacing I_m from (9) into (7) and simplifying (A2) (see Appendix A) is obtained. The inductor v_{Lf} voltage can be expressed as

$$v_{L_f}(\theta) = \omega L_f \frac{d}{d\theta} I_{in}(\theta) \tag{10}$$

Now,

$$v_{L_f} = \begin{cases} V_{in} \text{ if } 0 \le \theta < 2\pi D \\ V_{in} - v_s(\theta) \text{ if } 2\pi D \le \theta \le \theta \end{cases} \tag{11}$$

Now, considering the initial conditions, the current through L_f can be written as expressed in (A3) (see Appendix A). Now, $f_n(\theta)$ can be written as

$$f_n(\theta) = \frac{1}{\omega L_f} \int_{(n-1)\pi}^{\theta} V_{in} d\theta \tag{12}$$

where (12) is extended in (A4) (see Appendix A). If n is odd and m is even, by generalizing, (A4) and (A5) (see Appendix A) can be obtained for n and m, respectively.

3.2.3. Step 3

The boundary value of the input inductor can be determined by the following:

$$\Delta I_{in} = I_{in}(2\pi D) - I_{in}(0) = \frac{2\pi D V_{in}}{\omega L_{f\_boundary}} \tag{13}$$

which gives

$$L_{f\_boundary} = \frac{2\pi D V_{in}}{\omega \Delta I_{in}} \tag{14}$$

Now, the ripple current can be measured as

$$\Delta I_{in} = I_{in}(2\pi D) - I_{in}(2\pi) \tag{15}$$

Substituting the values of I_{in} from (A4) and (A5) and simplifying, the following is obtained:

$$\Delta I_{in} = \frac{\sqrt{\frac{2P_{out,rms}}{R_L}}\left(D^2 - 2\pi D + \pi\right) + 2\pi\omega V_{in} C_{in}(D-1)(2D-1)}{(D-1)\omega^2 C_{in} L_f} \tag{16}$$

3.2.4. Step 4

(a) *Case 1: The input average current and the input capacitance for N ≈ 1*

Now, if $N \approx 1$, the current is always positive and the inverter operates in close proximity of the BCM with high ripple current. The theoretical input current waveform is shown in Figure 3. In this case, the average current can be defined as

$$I_{in\_avg\_case1} = \frac{1}{2\pi}\left(\int_0^{2\pi D} I_{in\_1}(\theta)d\theta + \int_{2\pi D}^{2\pi} I_{in\_2}(\theta)d\theta\right) \tag{17}$$
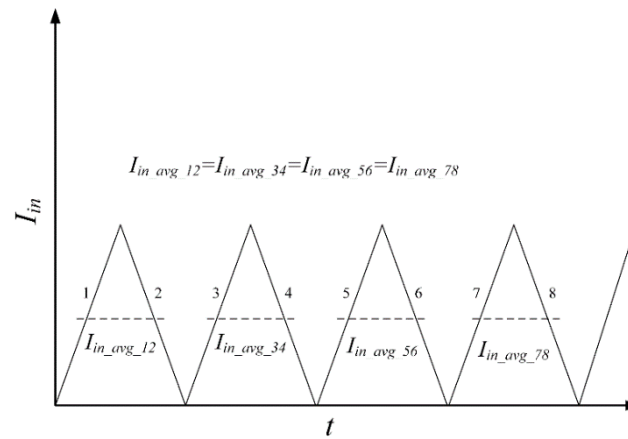
Figure 3. The theoretical input current when $N \approx 1$ and $D = 0.50$. Assume usual units for all parameters.

Now, simplifying (17) and using (A6)-(A7), (A8) can be obtained, which is shown in the Appendix A; where

$$A = \sqrt{2}\pi(D-1)\cos\varphi\left(1-\sqrt{2}\right) + \sin\varphi$$

$$B = \cos\varphi + \pi(D-1)\sin\varphi$$

$$C = -\sin\varphi - \pi(D-1)\cos\varphi$$

Again, from (3), (A9) (see Appendix A) is obtained. Alternatively, the average current ($I_{in\_avg\_case1\_alt}$) can be found (while $n = 5$ and $m = 6$) as shown in (A10) (see Appendix A). Accordingly, solving and simplifying (A10), (A11) (see Appendix A) is obtained, where

$$A' = \pi(D+3)\cos\varphi - \sin\varphi$$

$$B' = \cos\varphi + \pi(D+3)\sin\varphi$$

Now, the output power of the converter is

$$P_{out,rms} = \left(\frac{I_m}{\sqrt{2}}\right)^2 R_L = \frac{\left(\frac{V_{out,peak}}{\sqrt{2}}\right)^2}{R_L} \tag{18}$$

Now, I_m from (9) for *case 1* is

$$I_m = \frac{2\pi I_{in\_avg\_case1}(1-D)}{\cos(2\pi D + \varphi) - \cos\varphi} \tag{19}$$

Replacing from (19) in (18), $P_{out,rma}$ is obtained as demonstrated in (A12) (see Appendix A). Then, (A12) is solved for C_{in}, where N_1 and D_1 are demonstrated in (A13) and (A14) (see Appendix A).

$$C_{in\_case1} = \frac{N_1}{D_1} \tag{20}$$

The negative quotient of C_{in_case1} is neglected.

(b)   *Case 2: The input average current and the input capacitance for $1.5 < N < 3$:*

In this case, the input inductor is slightly greater than the $L_{f\_boundary}$ (approximately 1.5 to 2.5 times of $L_{f\_boundary}$). The $L_{f\_boundary}$, which is calculated from (14), is 50 µH and 55 µH at

D = 0.55 and 0.50, respectively. The theoretical input current waveform is shown in Figure 4. The current is always positive and the inverter operates at the continuous conduction mode (CCM) with high current ripple. The average current $I_{in\_avg\_case\_alt}$ as derived in (29) is appropriate. However, due to the transient nature of the input current, $I_{in\_avg\_sum34}$ is determined to define the input current more accurately.
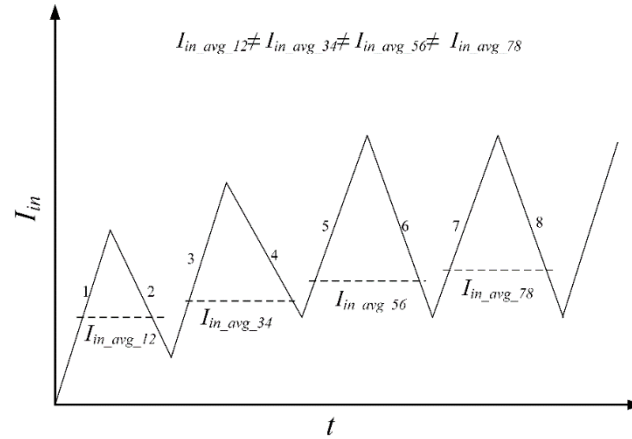

Figure 4. The theoretical input current when $1 < N < 3$ and D = 0.50. Assume usual units for all parameters.

For a better understanding, $I_{in\_avg\_78}$ is derived in (A15), where

$$A' = \pi(D+3)\cos\varphi - \sin\varphi$$

$$B' = \cos\varphi + \pi(D+3)\sin\varphi$$

(21)

The current is shown in Figure 5. Now, using (21) and (A16) (see Appendix A) is solved for C_{in} as demonstrated in (A17) (see Appendix A). The negative quotient of C_{in_case2} is neglected.

(c)　Case 3-The input average current and the input capacitance for $N \geq 3$:
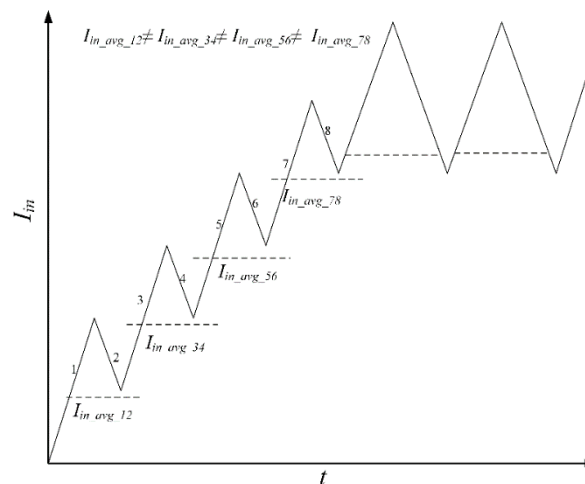

Figure 5. The theoretical input current when $N > 3$ and D = 0.50. Assume usual units for all parameters.

In this case, the input inductor is greater than the $L_{f\_boundary}$ (approximately 3 to 5 times of $L_{f\_boundary}$). The $L_{f\_boundary}$, which is calculated from (14), is 50 μH and 55 μH at D = 0.55 and

0.50, respectively. The theoretical input current waveform is shown in Figure 5. The current is always positive and the inverter operates at the continuous conduction mode (CCM) with low current ripple. Moreover, in this case, $I_{in\_avg\_case2}$ is sufficient. However, $I_{in\_avg\_15-16}$ is determined to define the input current more accurately. The C_{in_case3} is shown in (A20).

Hence,

$$I_{in\_avg\_case3} = I_{in\_avg\_case2} = I_{in\_avg\_78}$$

$$I_{in\_avg\_case3\_alt} = I_{in\_avg\_15-16} \tag{22}$$

Replacing values in (22) and simplifying, (A18) (see Appendix A) is obtained.

3.2.5. Step 5

The switch voltage can be determined from (3), (6) and (9). Now, if $n = 6$, solving for $dv_s/d\theta = 0$,

$$\theta_{pk} = -\varphi - \arcsin\left(\frac{1}{2\pi(D-1)}\right) \tag{23}$$

Replacing θ_{pk} from (23) into (A19) (see Appendix A) gives the peak switch voltage,

$$v_{s\_pk} = \frac{1}{2\pi\omega C_{in}(D-1)}\sqrt{\frac{2P_{out,rms}}{R_L}}\left(\left(\sqrt{4\pi^2(D-1)^2-1}\right)+\arcsin\left(\frac{1}{2\pi(D-1)}\right)+\varphi\right) \tag{24}$$

The switch current,

$$I_S(\theta) = I_{in} - I_m \sin(\theta+\varphi) \tag{25}$$

Replacing I_{in} from (5),

$$I_S(\theta) = \frac{I_m\left(\cos(2\pi D+\varphi)-\cos\varphi\right)}{2\pi(1-D)} - I_m \sin(\theta+\varphi) \tag{26}$$

The current peaks at

$$\theta = 2\pi D \tag{27}$$

Hence, replacing from (23) and (24) in (26),

$$i_{s\_pk} = \frac{\sqrt{\frac{2P_{out,rms}}{R_L}}\left(\pi(D-1)\sin(2\pi D+\varphi)-\frac{\cos\varphi}{2}+\frac{\cos(2\pi D+\varphi)}{2}\right)}{\pi(D-1)} \tag{28}$$

4. Analysis of The Model Parameters

4.1. The Phase Difference (φ):

The phase difference between the output voltage and current is given in (8). Now, if $D = 0$, $\varphi = \pi$. Again, if $D = 1$, φ is undefined (0/0).

In Figure 6, φ is plotted against D. At $D = 0$, φ is maximum at π. As D increases, the phase difference decreases.
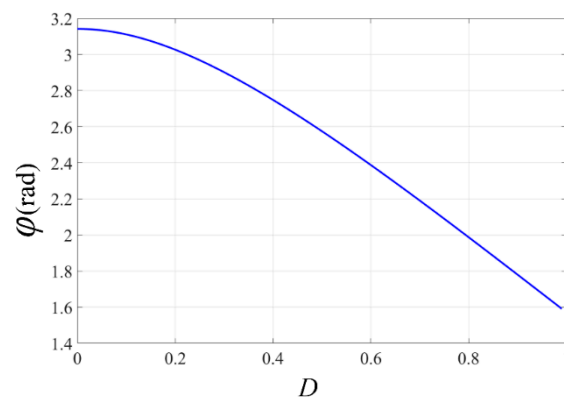
Figure 6. The phase difference against D at V_{in} = 15 V, V_{out_peak} = 20 V, P_{out_rms} = 10 W and f_s = 150 kHz.

4.2. *The Input Current Ripple*

The input current ripple decreases with increasing size of L_f.

In Figure 7, the input current ripple percentage is demonstrated against L_f. As L_f decreases, the ripple percentage increases according to (13). However, the input current (I_{in}) remains positive as long as $L_f > L_{f\_boundary}$.
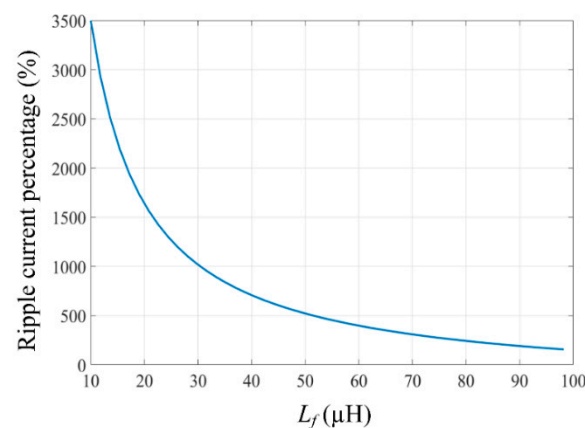

Figure 7. L_f vs M (input current ripple percentage) at D = 0.55, V_{in} = 15 V, V_{out} = 20 V, P_{out} = 10 W, C_{in} = 13 nF and f_s = 150 kHz.

4.3. *The Input Capacitance (C_{in})*

4.3.1. Case 1

In Figure 8a,b, C_{in_case1} is plotted against D and L_f, respectively, while V_{in} = 15 V, V_{out_peak} = 20 V, P_{out_rms} = 10 W and f_s = 150 kHz. As obvious from Figure 9a, C_{in_case1} is always positive for $D_{cr} \geq 0.52$, $D_{cr} \geq 0.48$ and $D_{cr} \geq 0.41$, while L_f = 50, 55 and 70 µH, respectively. In Figure 8b, C_{in_case1} is positive for $L_{f\_cr} > 52.8$ and $L_{f\_cr} > 46.4$ for D = 0.55 and 0.50, respectively. To achieve ZVS/ZVDS, these critical duty ratio and input inductances have to be maintained with C_{in_case1} being chosen appropriately under the specified conditions.
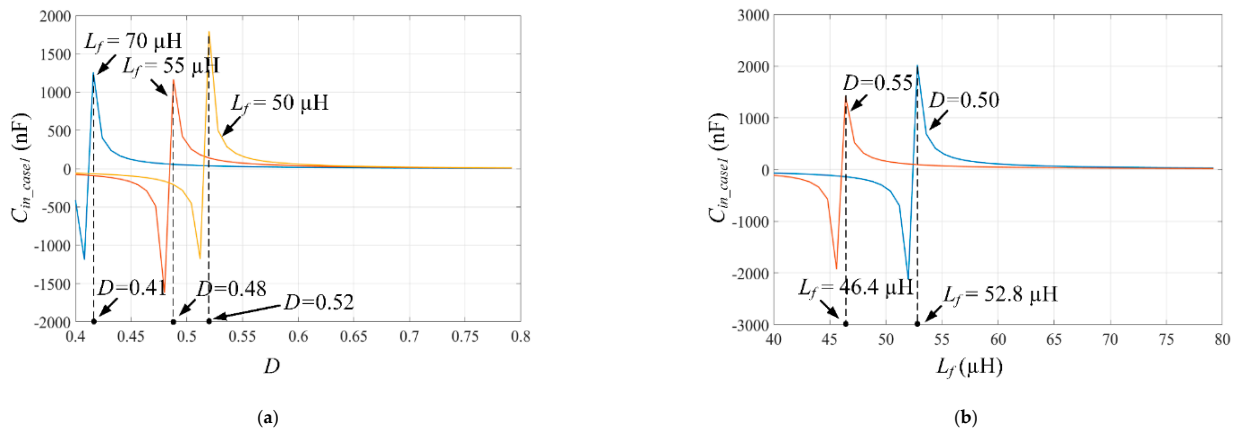
(a)

(b)

Figure 8. (**a**) C_{in_case1} vs D at L_f = 50, 55 and 70 μH (**b**) C_{in_case1} vs L_f at D = 0.50 and 0.55, while V_{in} = 15 V, V_{out_peak} = 20 V, P_{out} = 10 W and f_s = 150 kHz.

4.3.2. Case 2

In Figure 9a,b, C_{in_case2} is plotted against D and L_f, respectively, while V_{in} = 15 V, V_{out_peak} = 20 V, P_{out_rms} = 10 W and f_s = 150 kHz. As obvious from Figure 10a, C_{in_case2} is always positive for $D_{cr} \geq 0.52$, $D_{cr} \geq 0.54$ and $D_{cr} \geq 0.60$, while L_f = 100, 90 and 80 μH, respectively. In Figure 9b, C_{in_case2} is positive for L_{f_c} > 92.5 and L_{f_cr} > 105.2 for D = 0.55 and 0.50, respectively. To achieve ZVS/ZVDS, these critical duty ratio and input inductances have to be maintained with C_{in}_case1 being chosen appropriately under the specified conditions.
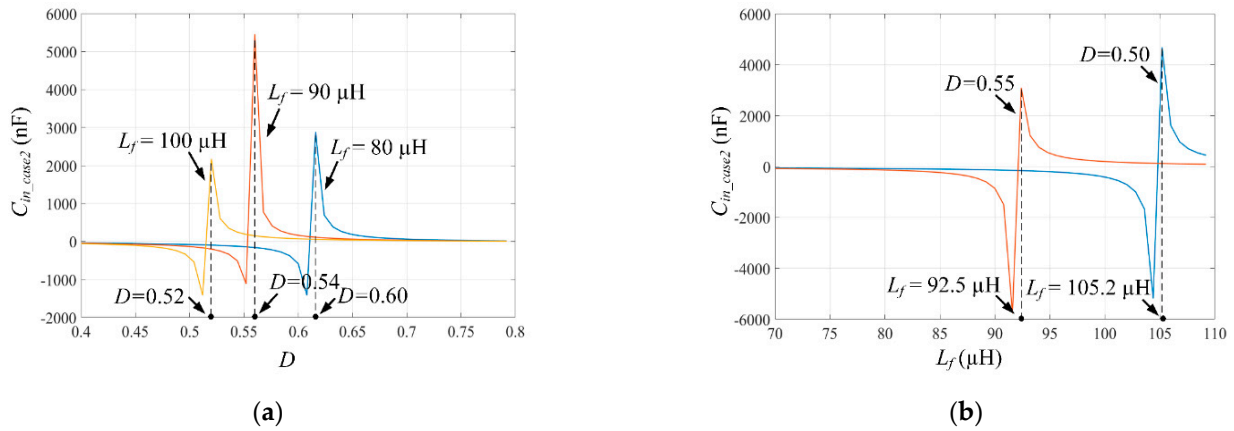

(**a**)

(**b**)

Figure 9. (**a**) C_{in_case2} vs D at L_f = 80, 90 and 100 μH (**b**) C_{in_case1} vs L_f at D = 0.50 and 0.55, while V_{in} = 15 V, V_{out_peak} = 20 V, P_{out} = 10 W and f_s = 150 kHz.

(**a**)

(**b**)
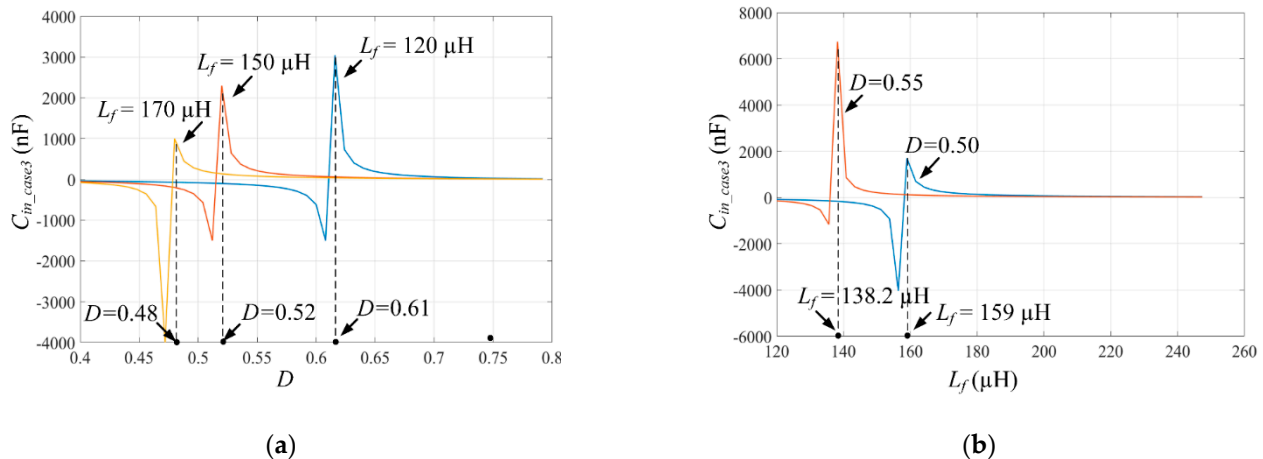
Figure 10. (**a**) C_{in_case3} vs D at L_f= 120, 150 and 170 μH (**b**) C_{in_case3} vs L_f at D = 0.50 and 0.55, while V_{in} = 15 V, V_{out_peak} = 20 V, P_{out} = 10 W and f_s= 150 kHz.

4.3.3. Case 3

In Figure 10a,b, C_{in_case3} is plotted against D and L_f, respectively, while V_{in} = 15 V, V_{out_peak} = 20 V, P_{out_rms} = 10 W and f_s = 150 kHz. As obvious from Figure 10a, C_{in_case3} is always positive for $D_{cr} \geq 0.48$, $D_{cr} \geq 0.52$ and $D_{cr} \geq 0.61$, while L_f = 170, 150 and 120 μH, respectively. In Figure 10b, C_{in_case2} is positive for $L_{f\_cr} > 138.2$ and $L_{f\_cr} > 159$ at D = 0.55 and 0.50, respectively. To achieve ZVS/ZVDS, these critical duty ratio and input inductances have to be maintained with C_{in_case3} being chosen appropriately under the specified conditions.

4.4. Peak Switch Voltage ($V_{s\text{-}pk}$)

The peak switch voltage (v_{s_pk}) from (24) is demonstrated in Figure 11. The rating of the switch should be 2–3 times the peak voltage for safe operation under the specified operating conditions. Moreover, from Figure 12b, it is obvious that the peak switch voltage can be lowered by lowering the output power at a given D and R_L. Similarly, it can be lowered by lowering the R_L at a given D and P_{out_rms} as obvious from Figure 12c. However, for both cases, the output voltage is also affected with v_{s_pk}.
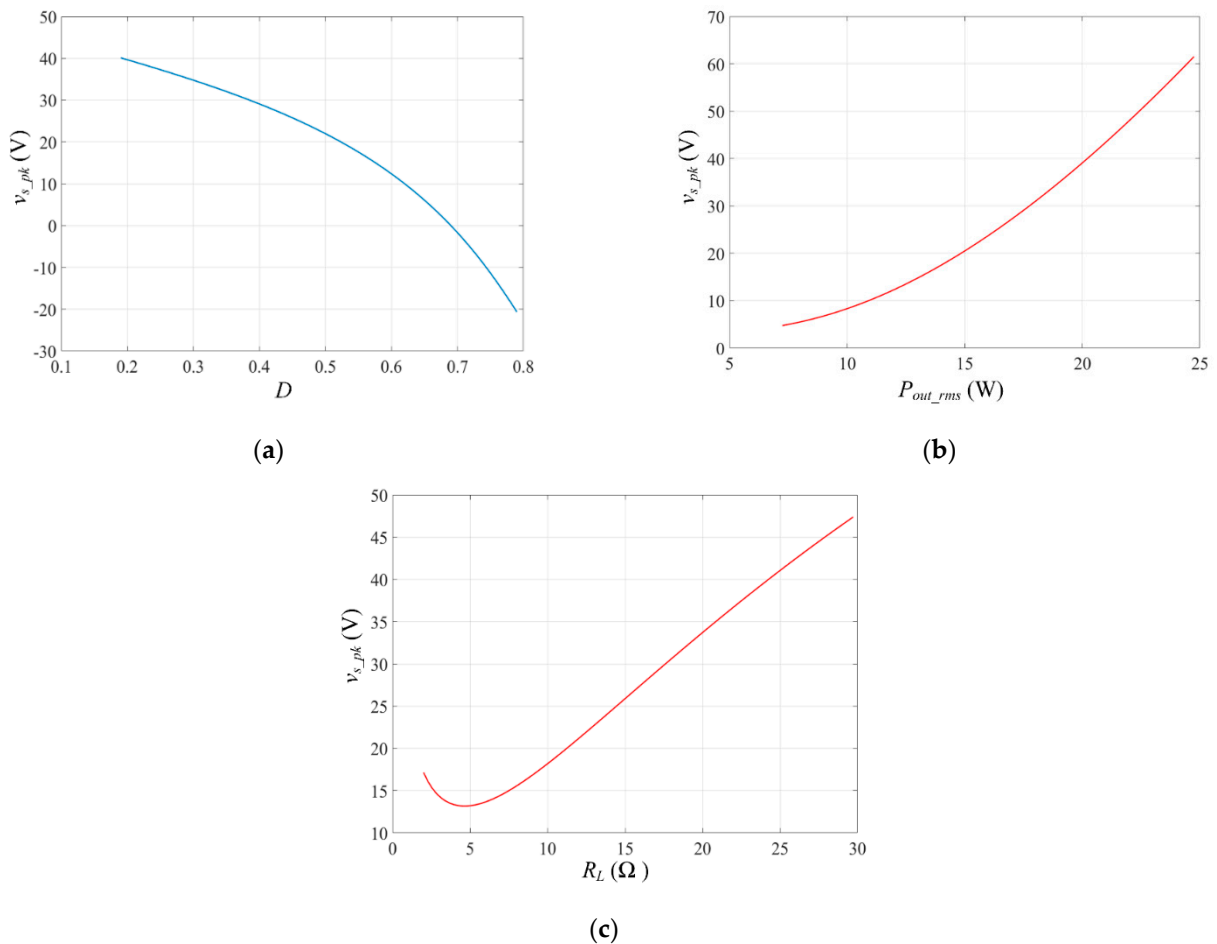

(**a**)

(**b**)

(**c**)

Figure 11. The peak switch voltage (v_{s_pk}) against (**a**) D while V_{in} = 15 V, V_{out_peak} = 20 V, R_L = 25 Ω, P_{out_rms} = 10 W and f_s = 150 kHz (**b**) P_{out_rms} while D = 0.5, V_{in} = 15 V, V_{out_peak} = 20 V, R_L = 25 Ω and f_s = 150 kHz (**c**) R_L while D = 0.5, V_{in} = 15 V, V_{out_peak} = 20 V, P_{out_rms} = 10 W and f_s = 150 kHz.
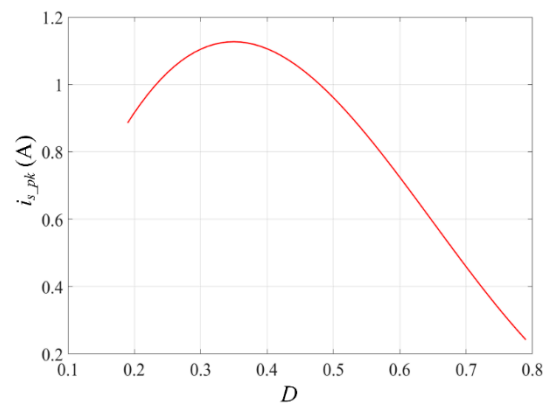
Figure 12. The peak switch current (i_{s_pk}) against *D*.

4.5. Peak Switch Current ($i_{s\text{-}pk}$)

The peak switch current (i_{s_pk}) from (28) is demonstrated in Figure 12. The peak current has a maximum in the mid region of *D* (0.3 to 0.5) and gradually decreases on both sides. Hence, given the optimum *D* = 0.5, the rating of the switch should be 2-3 times the peak current for safe operation.

5. Simulation and Experimental Verification

The class-E inverter is simulated in MATLAB Simulink environment to demonstrate the waveforms. Table 1 demonstrates the common parametric values.

The L_r and C_r is selected to maintain a high loaded Q_L factor ($Q_L \geq 10$), which is given as

$$Q_L = \frac{\omega L_r}{R_L} \tag{29}$$

Hence, the resonance frequency of the circuit is

$$f_r = \frac{1}{2\pi \sqrt{L_r C_r}} \tag{30}$$

Once, L_r is selected for the desired Q_L from (46), C_r can be determined.

Table 1. Specifications for Class-E Inverter.

Parameter	Value
V_{in}	15 V
V_{out_peak}	20 V
P_{out_rms}	10 W
D	0.50, 0.55
f_s, f_r	150 kHz
R_L	25 Ω
C_{out}	10 nF
C_{in}	13 nF and 72 nF
L_f	50 μH and 55 μH
L_r	1.3 mH
C_r	865.99355 pF

Case-1: Boundary Conduction Mode (N ≈ 1).

In this case, the input inductor is equal or close to the $L_{f\_boundary}$. The $L_{f\_boundary}$, which is calculated from (14), is 50 μH and 55 μH at *D* = 0.55 and 0.50, respectively. The output voltage and power of the inverter should demonstrate the specified value with minimal

error. In addition, the average input current from the simulation must concur with the analytical value from (A8). Accordingly, as C_{in} is implemented calculated from (A17), the ZVS/ZVDS should be executed.

The circuit is simulated at the designated parametric values stated in Table 1. The output voltage and power waveforms are shown in Figure 13 for $D = 0.50$. As opposed to the ideal lossless analytical model, the switch in the simulation induces a conduction loss across the ON resistance ($R_{ds\text{-}ON} = 0.015\ \Omega$).
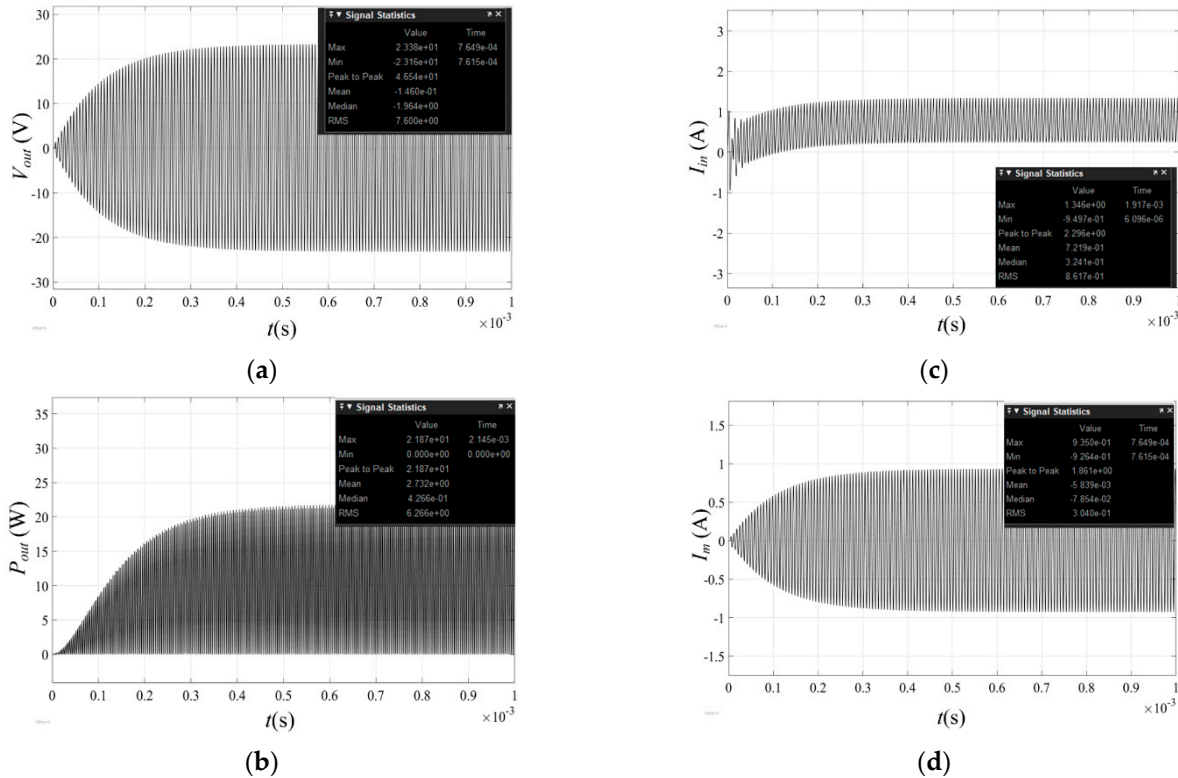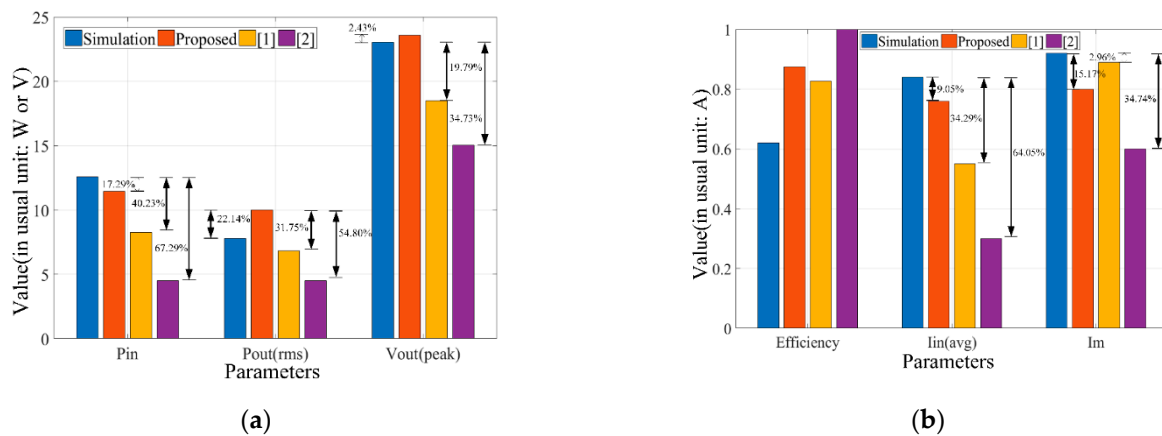
(**a**)

(**b**)

(**c**)

(**d**)

Figure 13. The (**a**) V_{out} at $D = 0.50$ (**b**) P_{out} at $D = 0.50$ (**c**) I_{in} at $D = 0.50$ (d I_m at $D = 0.50$.

In Figure 14, the analytical values of V_{in}, V_{out}, P_{in}, P_{out}, η, I_{in_avg}, I_m from the proposed model and [1,2] are stated along with the simulated results for $D = 0.55$ and 0.50. The percentage differences between the analytical and simulation results are calculated.
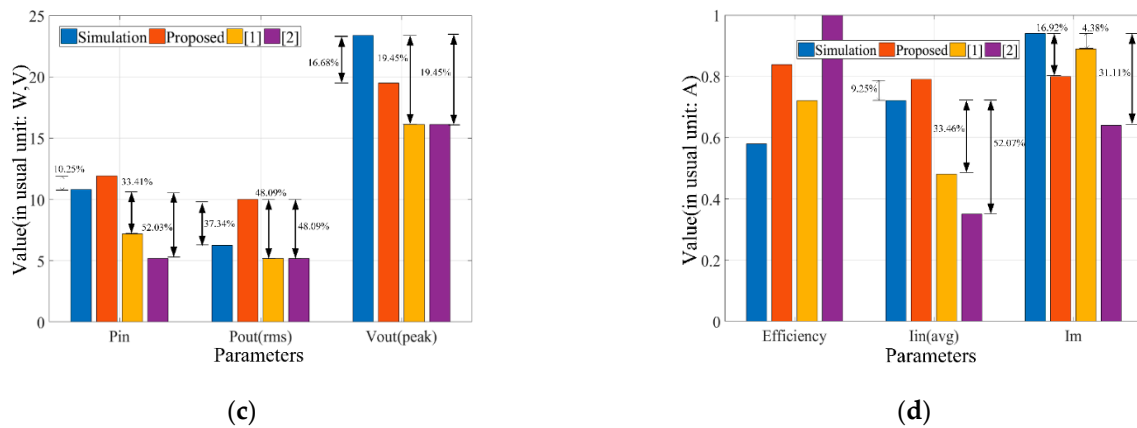
(**a**)

(**b**)

(**c**)

(**d**)

Figure 14. The comparison of the analytical and simulated results of (**a**) P_{in}, V_{out_peak} and P_{out_rms} at $D = 0.55$; (**b**) η, I_{in_avg} and I_m at $D = 0.55$; (**c**) P_{in}, V_{out_peak} and P_{out_rms} at $D = 0.50$; (**d**) η, I_{in_avg} and I_m at $D = 0.50$.

In Figure 14a, at $D = 0.55$, V_{out_peak} and P_{in} from the proposed model demonstrate a difference of 2.43% and 17.29% with the simulated value, respectively. For [1], these differences are maximum at 24.85% and 67.29%, respectively. In Figure 14b, the proposed model demonstrates a difference of 9.05% and 15.17% for I_{in_avg} and I_m while the maximum is 64.05% and 34.74%, respectively, for [1].

In Figure 14c, at $D = 0.50$, P_{in}, P_{out_rms} and V_{out_peak} demonstrate a difference of 10.25, 37.34 and 16.90%, respectively, for the proposed model. These parameters demonstrate a maximum difference of 52.03, 48.09 and 19.45%, respectively, for [1]. Again, in Figure 14d, a maximum difference of 52.07% in I_{in_avg} and 31.11% in I_m are observed for [1]. However, I_{in_avg} and I_m are most accurately determined by the proposed model and [2] demonstrating an error of 9.25% and 4.38%, respectively.

In Figure 15, the input average current for the proposed model, the model in [1,2] and for the simulation is demonstrated against D. As obvious, the optimum operating condition for the proposed model is $D \approx 0.43$ to 0.61. The shaded area stands for an error $\leq 10\%$.
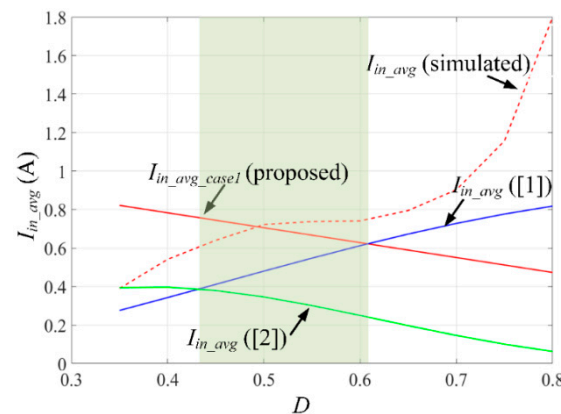

Figure 15. The input average current against D (case 1) while $V_{in} = 15$ V, $V_{out\_peak} = 20$ V, $P_{out\_rms} = 10$ W, $D = 0.50$, $f_s = 150$ kHz and $L_f = 50$ μH.

As stated previously, this model is accurate when the input inductor is equal or close to the boundary value ($L_{f\_boundary}$). Hence, the analytical value of I_{in} should closely match to that from the simulation. In Figure 16, the input average current for the proposed model is compared with [1,2] and the simulation against D. The results are summarized in Table

2. As obvious, the percentage error between the analytical and simulated values are maximum when the input current is negative (at low L_f). As L_f approaches to $L_{f\_boundary}$, the current always remains positive. Subsequently, the error is minimized.
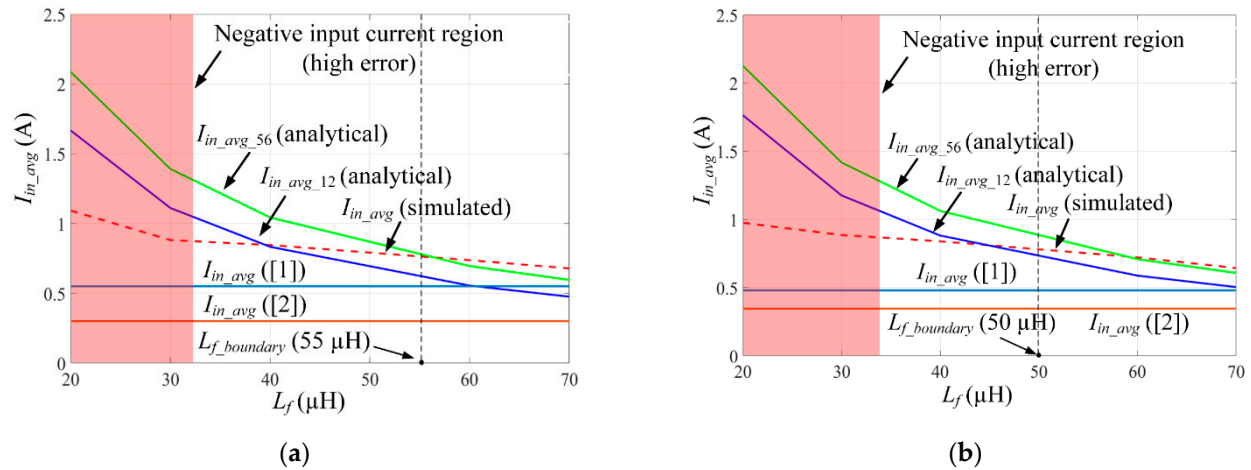

Figure 16. The average input currents vs L_f: the analytical (proposed, [1,2]) and simulated values at (**a**) $D = 0.55$ and (**b**) $D = 0.50$.

Table 2. The input current comparison against L_f ($I_{in\_avg\_12}$ and $I_{in\_avg\_56}$)

L_f (μH)	$I_{in\_avg\_12}$ (Analytical) (A)	$I_{in\_avg\_56}$ (Analytical) (A)	I_{in_avg} (Simulation) (A)	Error percentage ($I_{in\_avg\_12}$ and simulation) (%)	Error percentage ($I_{in\_avg\_56}$ and simulation) (%)	Ripple (Simulation) (%)
			$D = 0.55$			
20	1.6671	2.0871	1.0930	52.53	90.95	365.96
30	1.1114	1.3914	0.8819	20.65	57.77	249.46
40	0.8335	1.0435	0.8462	1.50	23.31	189.08
60	0.5557	0.6957	0.7180	22.60	3.10	111.42
70	0.4763	0.5963	0.6787	29.82	12.14	221.01
			$D = 0.50$			
20	1.7639	2.1261	0.9751	80.89	118.03	358.93
30	1.1759	1.4174	0.8859	32.73	59.99	237.04
40	0.8819	1.0630	0.8398	5.01	26.57	178.61
60	0.5880	0.7087	0.7219	18.54	1.82	145.44
70	0.5040	0.6075	0.6435	21.67	5.59	108.78

As L_f continues to increase from $L_{f\_boundary}$, $I_{in\_avg\_56}$ provides better approximation than $I_{in\_avg\_12}$. This is because of the transient nature of the current when the switch is turned ON. The error is as low as 1.5% (for $I_{in\_avg\_12}$) near $L_{f\_boundary}$ and 3.10% (for $I_{in\_avg\_56}$) at higher inductances. This is graphically shown in Figure 16a,b where the high error region (>20%) is shaded for $D = 0.55$ and $D = 0.50$, respectively. Accordingly, this region falls out of the scope of this model because of a significant error in approximating the average input current.

5.1. Case-2: The Continuous Conduction Mode (1 < N<3)

As stated earlier, the input inductor is slightly greater than the $L_{f\_boundary}$ (approximately 1.5 to 2.5 times of $L_{f\_boundary}$). The analytical values of V_{out}, P_{out}, I_{in_avg} and I_m are derived in Section 3.2. In this section, the average input current for the proposed model as stated in (A15) is calculated and compared with the simulation results.

In Figure 17, the input average current for the proposed model, the model in [1,2] and for the simulation is demonstrated against *D*. The optimum operating condition for the proposed model is $D \approx 0.50$ to 0.63. The shaded area stands for an error ≤10%.

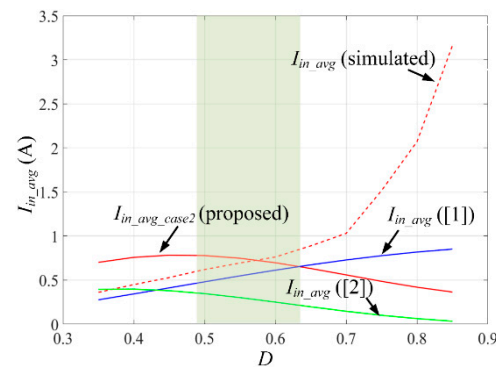**Figure 17.** The input average current against *D* (case 2) while V_{in} = 15 V, V_{out_peak} = 20 V, P_{out_rms} = 10 W, *D* = 0.50, f_s= 150 kHz and L_f= 100 μH.

In Figure 18, the input average current for the proposed model is compared with [1,2] and the simulation against *D*. The analytical and simulation results are summarized in Table 3. Owing to the transient nature of the input current, $I_{in\_avg\_56}$ gives rise to significant error in tracking the simulated values. The error becomes maximum, i.e., 44% and 36% at *D* = 0.55 and 0.50, respectively, for L_f = 110 μH. However, $I_{in\_avg\_sum34}$ provides a better approximation of the input current as L_f continues to increase. The minimum error of 0.36% and 16 % is recorded at *D* = 0.55 and 0.50, respectively, for L_f = 110 μH. The results are graphically shown in Figure 18a,b where the lower error region (≤10%) is shaded.
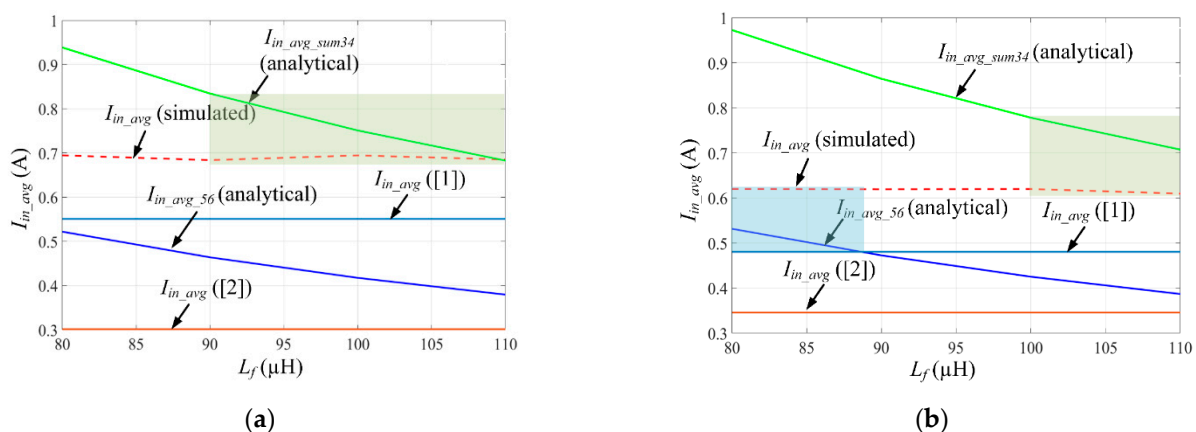

(**a**)   (**b**)

Figure 18. The average input currents vs L_f: the analytical (proposed, [1,2]) and simulated values at (**a**) *D* = 0.55 and (**b**) *D* = 0.50.

Table 3. The input current comparison against L_f ($I_{in\_avg\_56}$ and $I_{in\_avg\_sum34}$)

				D = 0.55		
L_f (μH)	$I_{in\_avg\_56}$ (Analytical)	$I_{in\_avg\_sum34}$ (Analytical)	I_{in_avg} (Simulation) (A)	Error percentage ($I_{in\_avg\_56}$ and simulation)	Error percentage ($I_{in\_avg\_sum34}$ and simulation)	Ripple (Simulation) (%)

	(A)	(A)		(%)	(%)	
80	0.5218	0.9385	0.6945	24.86	35.13	115.19
90	0.4638	0.8343	0.6837	32.16	21.70	95.07
100	0.4174	0.7508	0.6944	39.89	8.12	86.40
110	0.3795	0.6826	0.6851	44.60	0.36	80.28
			D = 0.50			
L_f (µH)	$I_{in\_avg\_56}$ (Analytical) (A)	$I_{in\_avg\_sum34}$ (Analytical) (A)	I_{in_avg} (Simulation) (A)	Error percentage ($I_{in\_avg\_56}$ and simulation) (%)	Error percentage ($I_{in\_avg\_sum34}$ and simulation) (%)	Ripple (Simulation) (%)
80	0.5315	0.9725	0.6200	14.27	56.85	129.17
90	0.4725	0.8644	0.6193	23.70	39.57	129.03
100	0.4252	0.7780	0.6198	31.39	25.52	80.67
110	0.3868	0.7072	0.6096	36.54	16.01	78.74

5.2. Case-3: The Continuous Conduction Mode (N > 3)

For case 3, the input inductor is greater than the $L_{f\_boundary}$ (approximately 2.5 to 5 times of $L_{f\_boundary}$). The analytical values of V_{out}, P_{out}, I_{in_avg} and I_m are derived in Section 3.2. In this section, the average input current for the proposed model as stated in (A19) is calculated and compared with the simulation results. In Figure 19, the input average current for the proposed model, the model in [1,2] and for the simulation is demonstrated against D. The optimum operating condition for the proposed model is $D \approx 0.50$ to 0.63. The shaded area stands for an error ≤10%.
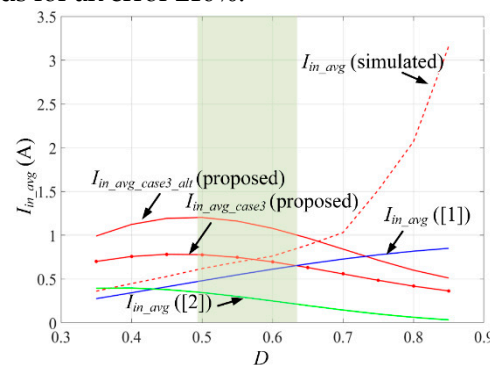

Figure 19. The input average current against D (case 3) while V_{in} = 15 V, V_{out_peak} = 20 V, P_{out_rms} = 10 W, D = 0.50, f_s = 150 kHz and L_f = 200 µH.

In Figure 20, the input average current for the proposed model is compared with [1,2] and the simulation against D. The analytical and simulation results are summarized in Table 4. Owing to the transient nature of the input current, $I_{in\_avg\_sum34}$ gives rise to significant error in tracking the simulated values at L_f = 160 µH. Beyond the latter, $I_{in\_avg\_sum56}$ provides a better approximation of the input current than [1,2] as L_f continues to increase. The minimum error of 7.56% and 1.39% is recorded at D = 0.55, L_f = 180 and D = 0.50, L_f = 200, respectively. The results are graphically shown in Figure 20a,b where the lower error region (≤10%) is shaded.
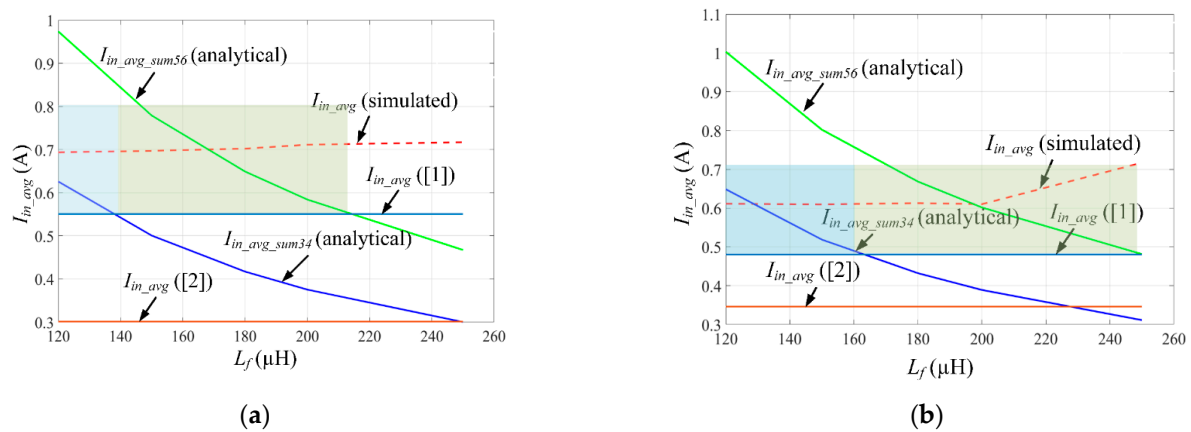
(**a**)

(**b**)

Figure 20. The average input currents vs L_f: the analytical (proposed, [1,2]) and simulated values at (**a**) $D = 0.55$ and (**b**) D = 0.50.

Table 4. The Input Current Comparison ($I_{in\_avg\_sum34}$ and $I_{in\_avg\_sum56}$).

L_f (μH)	$I_{in\_avg\_sum34}$ (Analytical) (A)	$I_{in\_avg\_sum56}$ (Analytical) (A)	I_{in_avg} (Simulation) (A)	Error percentage ($I_{in\_avg\_sum34}$ and simulation) (%)	Error percentage ($I_{in\_avg\_sum56}$ and simulation) (%)	Ripple (Simulation) (%)
			$D = 0.55$			
120	0.6257	0.9735	0.6936	9.78	40.35	72.08
150	0.5006	0.7788	0.6970	28.17	11.73	60.25
180	0.4171	0.6490	0.7021	40.59	7.56	54.12
200	0.3754	0.5841	0.7112	47.21	17.87	35.15
250	0.3003	0.4673	0.7169	58.11	34.81	27.89
			$D = 0.50$			
120	0.6484	1.0027	0.6111	6.10	64.08	65.45
150	0.5187	0.8021	0.6095	14.89	31.59	49.22
180	0.4322	0.6684	0.6128	29.47	9.07	48.95
200	0.3890	0.6016	0.6101	36.23	1.39	42.61
250	0.3112	0.4813	0.7169	56.59	32.86	27.80

The switch voltage and current waveforms are shown in Figure 21a,b for $D = 0.50$ and 0.55, respectively, for *case 1*. As expected, the switch voltage is either zero or negative at constant dv_s/dt. In Figure 21, the switch voltage and current waveforms are multiplied to measure the turn off losses. However, the exact switching loss would be nearly impossible to calculate from both a theoretical and simulation perspective. Instead, a very accurate relative estimate has been made from the simulated waveforms. As observed, the turn off loss ($P_{switching\_loss\_rms}$) is approximately 0.72, 1.2 and 1.93% of the output power (P_{out_rms} = 7.786 W) for $D = 0.50$ and 0.55, respectively. In all cases, the turn on loss is negligible. The results are accumulated in Table 5 below.
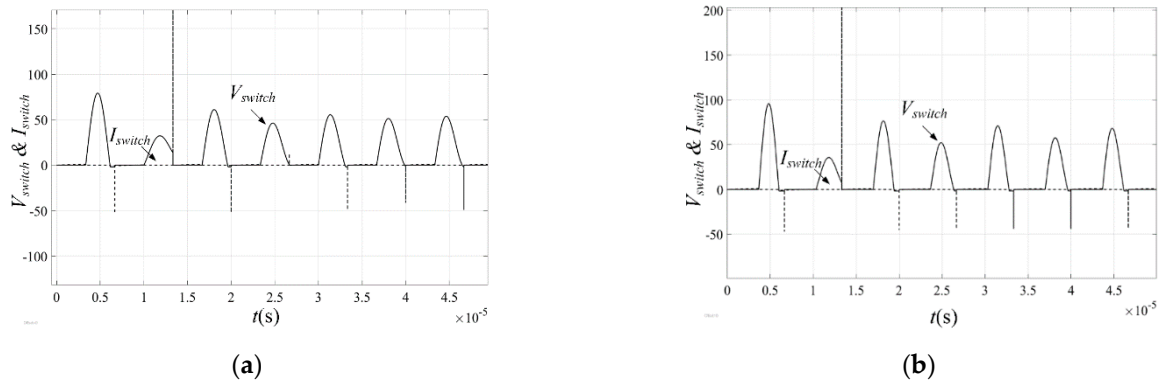
(**a**)

(**b**)

Figure 21. *Case 1*: (**a**) The switching waveforms at D = 0.50, L_f = 50 µH and C_{in} = 12 nF (**b**) The switching waveforms at D = 0.55, L_f = 55 µH and C_{in} = 9 nF.

The switch voltage and current waveforms are shown in Figure 22a,b for D = 0.50 and 0.55, respectively, for *case 2*. As expected, the switch voltage is either zero or negative at constant dv_s/dt. In Figure 22, the switch voltage and current waveforms are multiplied to measure the turn off losses. As observed, the turn off loss ($P_{switching\_loss\_rms}$) is approximately 0.60, 1.08 and 1.52% of the output power (P_{out_rms} =7.786 W) for D = 0.50 and 0.55, respectively. In all cases, the turn on loss is negligible. The results are accumulated in Table 5.

(**a**)
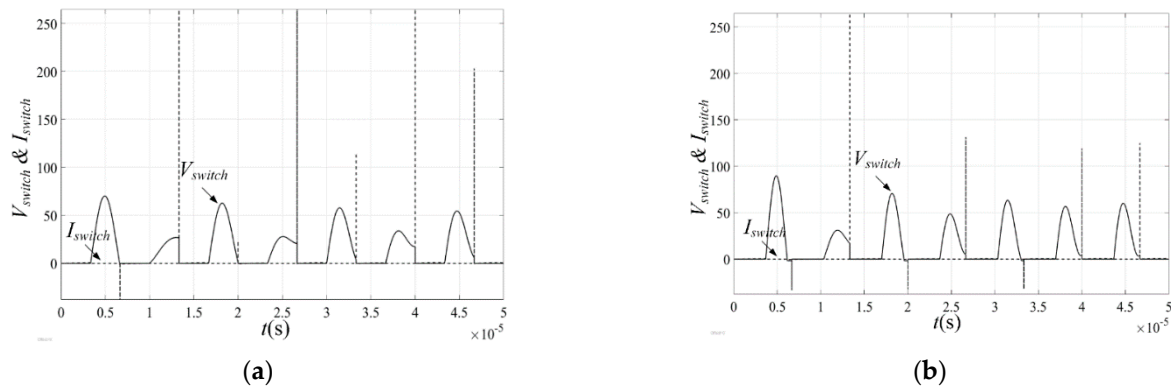

(**b**)

Figure 22. *Case 2*: (**a**) The switching waveforms at D = 0.50, L_f = 80 µH and C_{in} = 10 nF (**b**) The switching waveforms at D = 0.55, L_f = 100 µH and C_{in} = 5 nF.

The switch voltage and current waveforms are shown in Figure 23a,b for D = 0.50, 0.55 and 0.60, respectively, for *case 3*. As expected, the switch voltage is either zero or negative at constant dv_s/dt. In Figure 23, the switch voltage and current waveforms are multiplied to measure the turn off losses. As observed, the turn off loss ($P_{switching\_loss\_rms}$) is approximately 0.56, 0.20 and 1.27 % of the output power (P_{out_rms} = 7.786 W) for D = 0.50 and 0.55, respectively. In all cases, the turn on loss is negligible. The results are accumulated in Table 5 below.
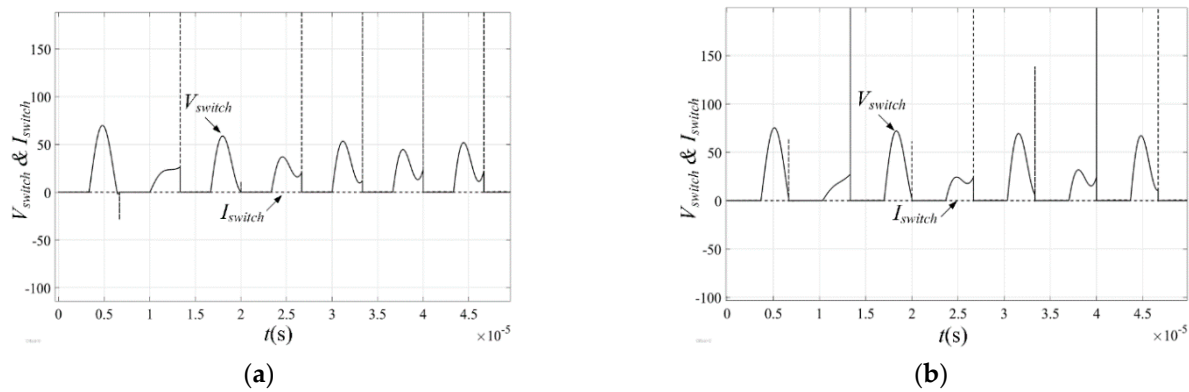
(a) (b)

Figure 23. *Case 3*: (**a**) The switching waveforms at *D* = 0.50, *L_f* = 180 μH and *C_in* = 4 nF (**b**) The switching waveforms at *D* = 0.55, *L_f* = 180 μH and *C_in* = 4 nF.

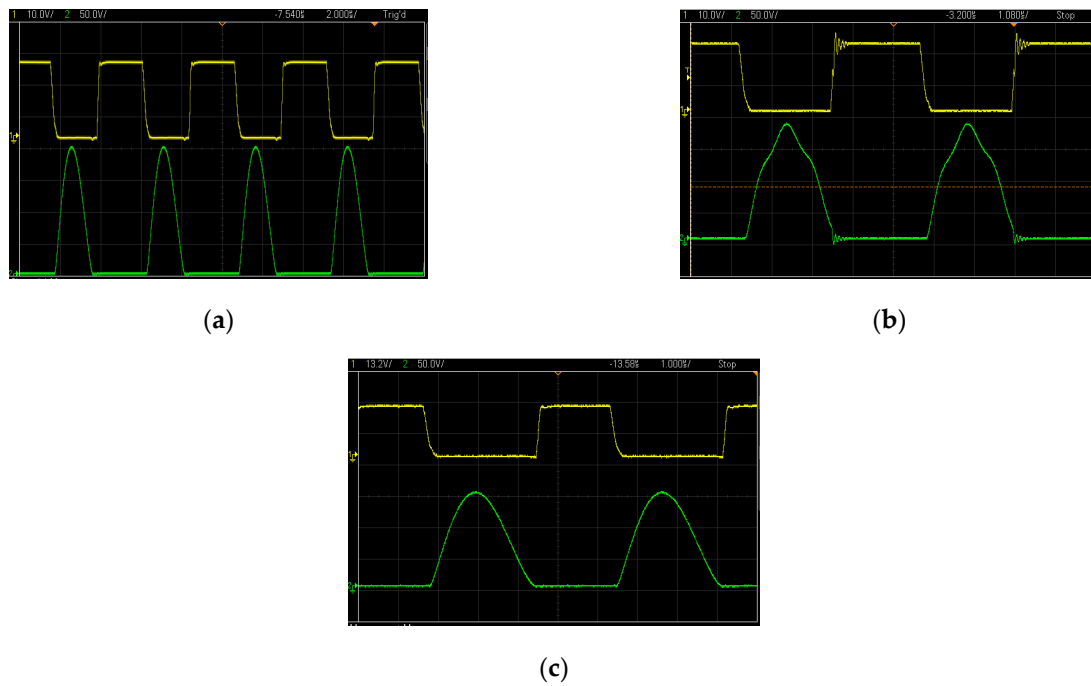In Figure 24, the switching waveforms reconfirms the ZVS achievement for case 1, 2 and 3.

(a) (b)

(c)

Figure 24. The switching waveforms at *Case 1*: (**a**) *D* = 0.50, *L_f* = 50 μH and *C_in* = 4 nF; *Case 2*: (**b**) *D* = 0.50, *L_f* = 80 μH and *C_in* = 10 nF; *Case 3*: (**c**) *D* = 0.50, *L_f* = 180 μH and *C_in* = 4 nF.

Table 5. The Approximate Switching Losses in *Case 1, 2* and *3*.

Case	D	L_f (μH)	C_{in} (nF)	$P_{switching\_loss\_rms}$ (mW)	Percentage Loss (%)
	0.50	50	12	56.43	0.72
1	0.55	55	9	93.95	1.20
	0.60	70	5	150.8	1.93
	0.50	80	10	46.76	0.60
2	0.55	100	5	84.08	1.08
	0.60	80	5	118.7	1.52
	0.50	180	4	43.83	0.56
3	0.55	180	4	15.29	0.20
	0.60	200	2	99.33	1.27

6. Conclusions

In this paper, the class-E inverter is modeled and analyzed for ZVS/ZVDS implementation. The modeling is based upon determining the input current to the inverter for various input inductances and state of ripple current under a specified condition. A comprehensive simulation and experimental testing are performed to support the proposed analytical model. Eventually, as opposed to the existing models, the proposed model can determine the input current, input/output power, efficiency more accurately. The percentage of error is also determined for different size of the input inductor and the duty ratio. For most of the part, the percentage error increases with increasing input inductor size at higher duty ratio and decreases at lower duty ratio. This input current is also used to determine the input capacitance of the inverter to aid the ZVS/ZVDS execution. It is observed that the percentage loss is <2% for all cases. In general, the results demonstrate that the proposed model is in better agreement with the test results as compared with the other existing models regardless of the input inductance and the input ripple current.

Appendix A

$$v_s(\theta) = \frac{I_m\left(\cos\left(2\pi D+\varphi\right)-\cos\varphi\right)\left(2\pi D-\theta\right)-2\pi I_m\left(\cos\left(2\pi D+\varphi\right)-\cos\left(\theta+\varphi\right)\right)\left(D-1\right)}{2\pi\omega C_{in}\left(D-1\right)} \tag{A1}$$

$$v_s(\theta) = \frac{\sqrt{\dfrac{2P_{out,rms}}{R_L}}\left(\left(2\pi D-\theta\right)\left(\cos\left(2\pi D+\varphi\right)-\cos\varphi\right)-2\pi\left(D-1\right)\left(\cos\left(2\pi D+\varphi\right)-\cos\left(\theta+\varphi\right)\right)\right)}{2\pi\omega C_{in}\left(D-1\right)} \tag{A2}$$

$$I_{in\_1}(\theta) = f_1(\theta)+0$$

$$I_{in\_2}(\theta) = f_2(\theta)+I_{in\_1}(2\pi D) = f_2(\theta)+f_1(2\pi D)+0$$

$$I_{in\_3}(\theta) = f_3(\theta)+I_{in\_2}(2\pi) = f_3(\theta)+f_2(2\pi)+f_1(2\pi D)+0 \tag{A3}$$

$$I_{in\_4}(\theta) = f_4(\theta)+I_{in\_3}(2\pi(1+D)) = f_4(\theta)+f_3(2\pi(1+D))+f_2(2\pi)+f_1(2\pi D)+0$$

$$I_{in\_5}(\theta) = f_5(\theta)+I_{in\_4}(4\pi) = f_5(\theta)+f_4(4\pi)+f_3(2\pi(1+D))+f_2(2\pi)+f_1(2\pi D)+0$$

$$f_n(\theta) = \frac{1}{\omega L_f}\int_{(n-1)\pi}^{\theta} V_{in}\,d\theta \tag{A4}$$

$$f_m(\theta) = \frac{1}{\omega L_f} \int\limits_{2\pi\left(\frac{m-2}{2}+D\right)}^{\theta} \left(V_{in} - \left(\frac{1}{(D-1)\pi\omega C_{in}} \left(\left(\left(\pi - \frac{\theta}{2}\right)\cos(2\pi D + \varphi) + \pi(D-1)\cos(\theta + \varphi) - \left(\pi D - \frac{\theta}{2}\right)\cos\varphi \right)\sqrt{\frac{P_{out,rms}}{R_L}} \right) \right) \right) d\theta \tag{A5}$$

$$I_{in\_n}(\theta) = f_n(\theta) + f_m\left(\pi(n-1)\right) + f_{n-2}\left(2\pi\left(\frac{n-3}{2}+D\right)\right) + f_m\left(\pi(n-3)\right) + \dots\dots \tag{A6}$$

$$I_{in\_m}(\theta) = f_m(\theta) + f_n\left(2\pi\left(\frac{(m-1)-1}{2}+D\right)\right) + f_{m-2}\left(\pi(m-2)\right) + f_n\left(2\pi\left(\frac{(m-3)-1}{2}+D\right)\right) + \dots\dots \tag{A7}$$

$$I_{in\_avg\_case1} = \frac{1}{\omega^2 L_f C_{in}} \left(\sqrt{\frac{2P_{out,rms}}{R_L}}(1-D)\left(A\cos^2(\pi D) + \sqrt{2}B\cos(\pi D)\sin(\pi D) + \sqrt{2}C + \pi(D-1)\cos\varphi \right) + 4V_{in}\pi\omega C_{in}\left(D^2 - D + \frac{1}{2}\right) \right) \tag{A8}$$

$$v_s(\theta) = \frac{1}{\omega C_{in}} \int\limits_{2\pi\left(\frac{m}{2}-1+D\right)}^{m\pi} \left(\frac{\sqrt{\dfrac{2P_{out,rms}}{R_L}}\left(\cos(2\pi D + \varphi) - \cos\varphi\right)}{2\pi(1-D)} - \sqrt{\frac{2P_{out,rms}}{R_L}}\sin(\theta+\varphi) \right) d\theta \tag{A9}$$

$$I_{in\_avg\_case1\_alt} = \frac{1}{2\pi\omega L_f} \left(\int\limits_{0}^{2\pi(2+D)}\left(\int\limits_{0}^{2\pi(2+D)} V_{in}\,d\theta \right)d\theta + \int\limits_{2\pi(2+D)}^{6\pi}\left(\int\limits_{2\pi(2+D)}^{6\pi} \left(V_{in} - v_s(\theta)\right)d\theta \right)d\theta \right) \tag{A10}$$

$$I_{in\_avg\_case1\_alt} = \frac{1}{\omega^2 L_f C_{in}} \left(\sqrt{\frac{8P_{out,rms}}{R_L}}(D-1)\left(A'\cos^2(\pi D) - B'\cos(\pi D)\sin(\pi D) - 4\pi\cos\varphi + \sin\varphi \right) + 4V_{in}\pi\omega C_{in}\left(D^2 + D + \frac{5}{2}\right) \right) \tag{A11}$$

$$P_{out,rms} = \left(-\frac{\sqrt{\dfrac{P_{out,rms}}{2R_L}}(D-1) - \omega V_{in}C_{in}}{\omega^2 L_f C_{in}} \right)^2 \frac{2R_L\left(\pi(1-D)\right)^2}{\left(\cos(2\pi D + \varphi) - \cos\varphi\right)^2} = \frac{V_{out,peak}^2}{2R_L} \tag{A12}$$

$$N_1 = \left(\sqrt{P_{out,rms}}\,\pi(D-1)^2 \left(\begin{array}{c} \omega L_f\sqrt{R_L}\sqrt{1-\cos^2(\pi D)}\sqrt{1-\cos^2(\pi D + \varphi)}\left(\begin{array}{c} \left(\left(-1+\pi^2(D^2-2D+17)\right)\cos^2(\pi D) - 2\pi(D-1)\sin(\pi D)\cos(\pi D) - 16\pi^2 + 1\right)\cos^2(\pi D + \varphi) \\ -8\pi\sin(\pi D + \varphi)\cos(\pi D + \varphi)\left(-1+\cos^2(\pi D) + \pi(D-1)\sin(\pi D)\cos(\pi D)\right) - 16\pi^2\cos^2(\pi D) + 16\pi^2 \end{array} \right)^{\frac{1}{2}} V_{out,peak} \\ -4\sqrt{2}V_{in}R_L\pi^2(D-1)\left(D^2 + \frac{1}{2}\right)\cos(\pi D + \varphi)\left(\left(-\sin(\pi D) + \pi(D-1)\cos(\pi D)\right) - 4\pi\sin(\pi D)\sin(\pi D + \varphi)\right) \end{array} \right) \right) \tag{A13}$$

$$D_1 = 8\omega\left(-\frac{L_f^2 V_{out,peak}^2\omega^2\cos^2(\pi D + \varphi)\left(\cos^2(\pi D)-1\right)}{32} + \frac{L_f^2 V_{out,peak}^2\omega^2\cos^2(\pi D)}{32} + V_{in}^2 R_L^2\pi^4(D-1)^2\left(D^2 + \frac{1}{2}\right)^2 - \frac{L_f^2 V_{out,peak}^2\omega^2}{32} \right) \tag{A14}$$

$$I_{in\_avg\_case2} = I_{in\_avg\_78} = \frac{1}{2\pi}\left(\int\limits_{6\pi}^{2\pi(3+D)} I_{in\_7}(\theta)\,d\theta + \int\limits_{2\pi(3+D)}^{8\pi} I_{in\_8}(\theta)\,d\theta \right) \tag{A15}$$

$$I_{in\_avg\_case2} = \frac{1}{\omega^2 L_f C_{in}}\left(\sqrt{\frac{8P_{out,rms}}{R_L}}(D-1)\left(A'\cos^2(\pi D) - B'\cos(\pi D)\sin(\pi D) - 4\pi\cos\varphi + \sin\varphi \right) + 4V_{in}\pi\omega C_{in}\left(D^2 + \frac{1}{2}\right) \right) \tag{A16}$$

$$C_{in\_case2} = \frac{-\left(\pi(D-1)^2\left(\sin(\pi D + \varphi)\sin(\pi D) + \frac{1}{4} \right)\left(\sqrt{\dfrac{2P_{out,rms}}{R_L}}\pi R_L^2 V_{in}(D-1) + \dfrac{\omega L_f V_{out,peak}\sin(\pi D + \varphi)\sin(\pi D)}{2} \right) \right)}{\left(\omega\left(-\dfrac{\omega^2 L_f^2 V_{out,peak}^2\sin^2(\pi D + \varphi)\sin^2(\pi D)}{8} + +\pi^2 R_L^2 V_{in}^2(D-1)^2 \right) \right)} \tag{A17}$$

$$I_{in\_avg\_case3\_alt} = \frac{1}{\omega^2 L_f C_{in}} \left(\sqrt{\frac{8P_{out,rms}}{R_L}} (D-1) \left(A'' \cos^2(\pi D) - B'' \cos(\pi D) \sin(\pi D) - 14\pi \cos\varphi + \sin\varphi \right) + 4V_{in}\pi\omega C_{in} \left(D^2 - D + \frac{1}{2} \right) \right. \tag{A18}$$

$$v_s(\theta) = \frac{1}{\omega C_{in}} \int_{2\pi\left(\frac{m}{2}-1+D\right)}^{m\pi} \left(\frac{\sqrt{\frac{2P_{out,rms}}{R_L}} \left(\cos(2\pi D + \varphi) - \cos\varphi \right)}{2\pi(1-D)} - \sqrt{\frac{2P_{out,rms}}{R_L}} \sin(\theta + \varphi) \right) d\theta \tag{A19}$$

$$C_{in\_case3} = \frac{-\left(4\pi(D-1)^2 \left(\sin(\pi D + \varphi)\sin(\pi D) + \frac{3}{8} \right) \left(\sqrt{\frac{2P_{out,rms}}{R_L}} \pi R_L^2 V_{in}(D-1) + \frac{\omega L_f V_{out,peak} \sin(\pi D + \varphi)\sin(\pi D)\sqrt{R_L P_{out,rms}}}{2} \right) \right)}{\left(3\omega \left(-\frac{\omega^2 L_f^2 V_{out,peak}^2 \sin^2(\pi D + \varphi)\sin^2(\pi D)}{18} + \pi^2 R_L^2 V_{in}^2(D-1)^2 \right) \right)} \tag{A20}$$

References

1. Hayati, M.; Lotfi, A.; Kazimierczuk, M.K.; Sekiya, H. Analysis and Design of Class-E Power Amplifier With MOSFET Parasitic Linear and Nonlinear Capacitances at Any Duty Ratio. *IEEE Trans. Power Electron.* **2013**, *28*, 5222–5232.
2. Ayachit, A.; Corti, F.; Reatti, A.; Kazimierczuk, M.K. Zero-Voltage Switching Operation of Transformer Class-E Inverter at Any Coupling Coefficient. *IEEE Trans. Ind. Electron.* **2019**, *66*, 1809–1819.
3. Hayati, M.; Roshani, S.; Roshani, S.; Kazimierczuk, M.K.; Sekiya, H. Design of Class E Power Amplifier with New Structure and Flat Top Switch Voltage Waveform. *IEEE Trans. Power Electron.* **2018**, *33*, 2571–2579.
4. Sheikhi, M.; Hayati, A.; Grebennikov, A. Design Methodology of Class-E/F3Power Amplifier Considering Linear External and Nonlinear Drain–Source Capacitance. *IEEE Trans. Microw. Theory Tech.* **2017**, *65*, 548–554.
5. Hayati, M.; Sheikhi, A.; Grebennikov, A. Design and Analysis of Class E/F₃ Power Amplifier with Nonlinear Shunt Capacitance at Nonoptimum Operation. *IEEE Trans. Power Electron.* **2015**, *30*, 727–734.
6. Kessler, D.J.; Kazimierczuk, M.K. Power losses and efficiency of class-E power amplifier at any duty ratio. *IEEE Trans. Circuits Syst. I Regul. Pap.* **2004**, *51*, 1675–1689.
7. Thongsongyod, C.; Ekkaravarodome, C.; Jirasereeamornkul, K.; Boonyaroonate, I.; Higuchi, K. High step-up ratio DC-DC converter using Class-E resonant inverter and Class-DE rectifier for low voltage DC sources. In Proceedings of the 2016 International Conference on Electronics, Information, and Communications (ICEIC), Danang, Vietnam, 27–30 January 2016; pp. 1–4.
8. Niyomthai, S.; Sangswang, A.; Naetiladdanon, S.; Mujjalinvimut, E. Operation region of class E resonant inverter for ultrasonic transducer. In Proceedings of the 2017 14th International Conference on Electrical Engineering/Electronics, Computer, Telecommunications and Information Technology (ECTI-CON), Phuket, Thailand, 27–30 June 2017; pp. 435–438.
9. Rizo, L.; Ruiz, M.N.; García, J.A. Device characterization and modeling for the design of UHF Class-E inverters and synchronous rectifiers. In Proceedings of the 2014 IEEE 15th Workshop on Control and Modeling for Power Electronics (COMPEL), Santander, Spain, 22–25 June 2014; pp. 1–5.
10. Ma, K.; Chang, W.; Lee, Y. A simple CLASS-E inverter design for driving ultrasonic welding system. In Proceedings of the 2009 International Conference on Power Electronics and Drive Systems (PEDS), Taipei, Taiwan, 2–5 November 2009; pp. 894–896.
11. Ekbote, A.; Zinger, D.S. Comparison of Class E and Half Bridge Inverters for Use in Electronic Ballasts. In Proceedings of the Conference Record of the 2006 IEEE Industry Applications Conference Forty-First IAS Annual Meeting, Tampa, FL, USA, 8–12 October 2006; Volume 5, pp. 2198–2201.
12. Ashique, R.H.; Khan, M.M.; Shihavuddin, A.; Maruf, M.H.; Al Mansur, A.; ul Haq, M.A. A Novel Family of Class EF$_{nm}$ and E/F$_{nm}$ Inverter for Improved Efficiency. In Proceedings of the 2020 2nd International Conference on Sustainable Technologies for Industry 4.0 (STI), Dhaka, Bangladesh, 19–20 December 2020; pp. 1–6.
13. Aldhaher, S.; Yates, D.C.; Mitcheson, P.D. Modeling and Analysis of Class EF and Class E/F Inverters with Series-Tuned Resonant Networks. *IEEE Trans. Power Electron.* **2016**, *31*, 3415–3430.
14. Kaczmarczyk, Z.; Jurczak, W.A. Push–Pull Class-E Inverter with Improved Efficiency. *IEEE Trans. Ind. Electron.* **2008**, *55*, 1871–1874.
15. Kazimierczuk, M.K.; Jozwik, J. DC/DC converter with class E zero-voltage-switching inverter and class E zero-current-switching rectifier. *IEEE Trans. Circuits Syst.* **1989**, *36*, 1485–1488.
16. Li, Y.; Sue, S. Exactly analysis of ZVS behavior for class E inverter with resonant components varying. In Proceedings of the 2011 6th IEEE Conference on Industrial Electronics and Applications, Beijing, China, 21–23 June 2011; pp. 1245–1250.